Concurrent fluorescence and volumetric optoacoustic tomography of nanoagent perfusion and bio-distribution in solid tumors

Zhenyue Chen,[1,2,3] Xosé Luis Deán-Ben,[1,2,3] Nian Liu,[3,4] Vipul Gujrati,[3] Sven Gottschalk,[3] Vasilis Ntziachristos,[3,4] and Daniel Razansky[1,2,3,4,*]

[1]*Faculty of Medicine and Institute of Pharmacology and Toxicology, University of Zurich, Switzerland*
[2]*Institute for Biomedical Engineering and Department of Information Technology and Electrical Engineering, ETH Zurich, Switzerland*
[3]*Institute for Biological and Medical Imaging, Helmholtz Center Munich, Neuherberg, Germany*
[4]*Faculty of Medicine, Technical University of Munich, Germany*
**daniel.razansky@uzh.ch*

Abstract: Intravenously administered liposomes and other nano-sized particles are known to passively accumulate in solid tumors via the enhanced permeability and retention (EPR) effect, which is extensively explored toward the improvement of diagnosis and drug delivery in oncology. Agent extravasation into tumors is often hampered by the mononuclear phagocytic and renal systems, which sequester and/or eliminate most of the nanoparticles from the body. Dynamic imaging of the tumor microcirculation and bolus perfusion can thus facilitate optimization of the nanoparticle delivery. When it comes to non-invasive visualization of rapid biological dynamics in whole tumors, the currently available pre-clinical imaging modalities are commonly limited by shallow penetration, lack of suitable contrast or otherwise insufficient spatial or temporal resolution. Herein, we demonstrate the unique capabilities of a combined epi-fluorescence and optoacoustic tomography (FLOT) system for characterizing contrast agent dynamics in orthotopic breast tumors in mice. A liposomal indocyanine green (Lipo-ICG) preparation was administered intravenously with the time-lapse data continuously acquired during and after the injection procedure. In addition to the highly sensitive detection of the fluorescence agent by the epi-fluorescence modality, the volumetric multi-spectral optoacoustic tomography readings further enabled resolving deep-seated vascular structures with high spatial resolution and hence provided accurate readings of the dynamic bio-distribution of nanoparticles in the entire tumor in 3D. The synergetic combination of the two modalities can become a powerful tool in cancer research and potentially aid the diagnosis, staging and treatment guidance of certain types of cancer in the clinical setting.

1. Introduction

Nanoparticles injected into tumor-bearing animals are likely to leak into the extracellular matrix through the abnormal vessels formed during tumor growth. Such neo-vascular network is characterized by a hierarchical disorganization exhibiting a convoluted structure including irregular branching, arteriovenous shunts and a fenestrated endothelium with relatively large gaps between cells [1]. Particularly, mother vessels originating from normal venules and capillaries are composed of a thin layer of endothelial cells featuring abnormal hyper-permeability to plasma proteins [2]. This, along with the fact that blood flow is reduced by elevated levels of viscosity in such vessels, facilitates extravasation of nanoparticles smaller than ~200 nm [3,4]. Since most tumors lack effective lymphatic drainage, the nanoparticles remain in tissue and are considered to passively target the tumor via the so-called enhanced

permeability and retention (EPR) effect [5]. There are however two biological barriers that hamper nanoparticle delivery into the tumor. The first one is the renal system, which excretes molecules and nanoparticles with a hydrodynamic diameter smaller than ~5.5 nm [6]. The second barrier is the mononuclear phagocytic system consisting of a network of organs (particularly the liver and spleen) containing cells that can phagocytize larger nanoparticles [7]. A recent review on the literature on nanoparticle delivery to tumors from the last decade showed that only 0.7% (median) of the injected nanoparticles reach the target tumor (0.6% for passive targeting) [8]. Then, it appears that optimizing the nanoparticles to enhance the extravasation during the first passes through the tumor microvasculature is a key factor in achieving more efficient tumor targeting.

Medical imaging technologies have experienced major advancements in the last few decades and currently play an essential role in oncology [9,10]. The EPR effect was first described by visualizing the accumulation of an Evans blue complex with albumin into mouse tumor tissues [11], and imaging technologies continue to be widely used for a better characterization and understanding of this phenomenon [12]. X-ray imaging (planar or computed tomography (CT)), magnetic resonance imaging (MRI), nuclear medicine (single photon emission tomography (SPECT) and positron emission tomography (PET)), ultrasound (US) and optical imaging are routinely being used for the diagnosis, staging and treatment of cancer [13]. All these technologies offer certain capabilities for monitoring contrast agent perfusion and extravasation, but are also afflicted by several limitations. The generally low temporal resolution of tomographic imaging modalities such as CT, MRI and PET hinders proper characterization of the EPR dynamics [14]. US provides high-frame-rate imaging, but extravasation of most US contrast agents is commonly hindered by their large size [15]. Optical imaging methods, particularly fluorescence-based, can detect a large variety of contrast agents in real time with high sensitivity and further enable intraoperative monitoring of cancer-related surgeries [16].Yet, strong light scattering in biological tissues leads to loss of spatial resolution and inability to resolve depth. Optoacoustic (OA) imaging has emerged in the 2000s as a technology capable of providing functional and molecular imaging capabilities that can be used for visualizing fluorescent and non-fluorescent light-absorbing agents [17–24]. OA further enables high-resolution mapping of vascular networks [25], while state-of-the-art systems provide very high imaging rates in the order of hundreds to thousands of Hertz [26]. Overall, OA offers unique capabilities for cancer research and is growingly being used in small-animal studies aiming at providing new insights on tumor growth and development. A thorough comparison of the sensitivity limits of OA imaging with respect to other fluorescence-based optical imaging techniques is yet to be established [27], in particular in connection to detecting small amounts of nano-agents retained by (or targeted to) solid tumors.

Herein, we exploit the synergistic advantages of a combined two dimensional (2D) epi-fluorescence and real-time volumetric multi-spectral optoacoustic tomography (FLOT) system for high-frame-rate visualization of the dynamics of nanoparticles as they perfuse in the tumor microvasculature. Indocyanine green (ICG) was encapsulated into liposomes to form ~110 nm nanoparticles. The liposomal ICG (Lipo-ICG) solution was injected intravenously in mice featuring orthotopic breast tumors and a sequence of hybrid FLOT images was acquired at 10 frames per second. The system can efficiently analyze the pharmacokinetics of the particles early-on in circulation during the first passes of the bolus through the tumor vasculature. Additionally, it is shown that the suggested approach enables sensitive detection of extravasation at different time points as well as oxygen saturation mapping in the entire tumor volume.

2. Materials and methods

Hybrid epifluorescence and optoacoustic imaging system

The hybrid FLOT system used for mouse breast tumor imaging is depicted in Fig. 1(a). A custom-made fiberscope (Zibra Corporation, Westport, MA) was used to excite both fluorescence and optoacoustic responses and acquire epi-fluorescence images through the cylindrical cavity of a spherical ultrasound array [28]. The fiberscope consists of a 1.4 mm diameter optic image guide made of 100,000 fibers and an illumination bundle composed of 7 fibers having 600 μm core diameter and 0.4 numerical aperture (NA) each. An emission filter was placed in front of an electron multiplying charged-coupled device (EMCCD)-based camera (Andor Luca R, Oxford Instruments, UK) to selectively collect the fluorescence responses transmitted through the optic guide. The ultrasound array (Imasonic SaS, France) was used to collect OA signals with 512 piezocomposite elements having ~2.5 mm diameter, 5 MHz central frequency and ~100% detection bandwidth [29].The elements are uniformly distributed on a spherical surface with 40 mm radius and 140° angular coverage (1.3π solid angle). An optical parametric oscillator (OPO)-based short-pulsed laser (Innolas Laser GmbH, Germany) was guided through the illumination bundle of the fiberscope, simultaneously exciting OA and fluorescence responses.

Fluorescence and OA images were recorded for 15 minutes. The acquisition commenced ~20 s before the tail vein injection of Lipo-ICG. The wavelength and the pulse repetition frequency (PRF) of the laser were tuned to 780 nm and 10 Hz, respectively. One-minute duration FLOT data was additionally recorded at 30, 45 and 60 min post Lipo-ICG injection. For this, the excitation wavelength was set at 780 nm for fluorescence imaging while the corresponding OA data was recorded at five excitation wavelengths of 720, 755, 780, 820 and 855 nm.

Optoacoustic image reconstruction and multi-spectral unmixing

Three-dimensional optoacoustic images were obtained from the acquired time-resolved signals with a graphics processing unit (GPU) implementation of a back-projection formula [30]. Prior to reconstruction, the signals were deconvolved with the electrical impulse response of the transducer and band-pass filter to suppress low frequency bias and high frequency noise. The reconstructed images at different wavelengths were averaged and then further processed to unmix the distribution of the injected contrast agent and estimate the blood oxygen saturation levels. For this, a linear model assuming that the light fluence distribution does not significantly change with wavelength was used. Although more accurate approaches have been suggested [31], this method has shown to provide sufficient accuracy for mapping oxygen saturation levels for spherical transducer arrays and the relatively shallow depth of the tumors [32].

Animal models for the experiments

Experiments were performed with the MDA-MB-231 murine breast tumor model. Specifically, two 4-week old adult female athymic nude-Foxn1 nude mice (Harlan Laboratories LTD, Switzerland) were inoculated subcutaneously in the breast region next to the left hind leg (Fig. 1(b)) with 3 million cells in 30 μL PBS. The mice were imaged after tumors reached a size of approximately 10 mm diameter (10 days after inoculation). Tail-vein injection of 100 μl of 0.5 mg/ml Lipo-ICG solution in water was performed as described above. During the experiments, the mice were anesthetized with isoflurane (2.5% v/v for induction followed by 1.5-2.0% v/v) in 100% O2 at a flow rate of ~0.8 l/min. After completion of the measurements, the mice were euthanized while still being under anesthesia. Animal handling and experimentation were conducted in full accordance with the directives on animal experimentation of the Helmholtz Center Munich and with approval from the Government District of Upper Bavaria.

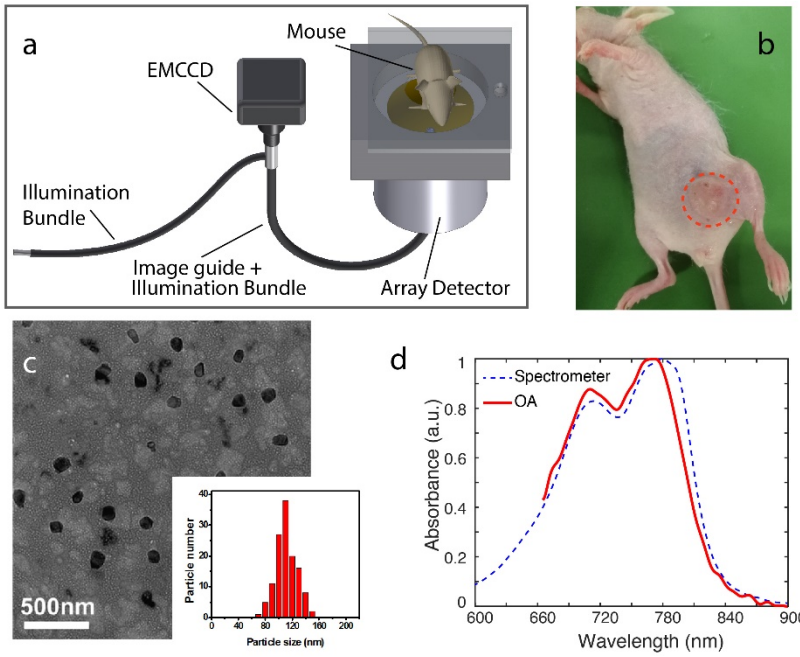

Fig. 1. Experimental set-up and Lipo-ICG characterization. (a) Schematic of the FLOT system. (b) Photograph of the mouse carrying the MDA-MB-231 breast tumor. (c) Electron microscope image of the Lipo-ICG contrast agent. (d) Spectrophotometer- and OA-based measurements of the absorption spectrum of Lipo-ICG with a concentration of 50 µg/ml.

Liposomal ICG preparation

Lipo-ICG was prepared using the reverse phase evaporation method [33]. In brief, 50 mg DSPC, 40 mg cholesterol and 5 mg DSPE-PEG2k were dissolved in 5 mL dichloromethane, while 5 mg ICG was separately dissolved in 10 mL Milli-Q water. These two solutions were mixed together and sonicated for 120 s. The organic solvent was subsequently evaporated from the mixture by rotary evaporation. An ivory emulsion was subsequently obtained. In order to remove the unentrapped ICG, the dispersion was subjected five times to ultrafiltration (MWCO = 100K, 5000 rpm, 10 min). The final dispersion was passed through an extruder with polycarbonate membrane filters (450 nm pore size). Transmission electron microscopy (TEM) image of the engineered Lipo-ICG with particle size in the 110 nm range is shown in Fig. 1(c). The encapsulation efficiency of ICG was 94.62 ± 0.74%, as measured after ultracentrifugation with a UV-visible spectrophotometer.

3. Results

We first compared the absorption spectrum of Lipo-ICG with a concentration of 50 µg/ml as measured by a conventional spectrophotometer (Ocean Optics Inc., USA) to its OA spectrum. While the spectrophotometer measurement featured an absorption peak at 780 nm wavelength, as expected for ICG in water, the peak was shifted by ~10 nm in the OA measurement (Fig. 1(d)). The discrepancy can be attributed to the fluorescence leakage into the light sensor during the absorbance measurement with the spectrophotometer.

Experimental results of time-lapse imaging of the Lipo-ICG perfusion in mouse tumors are presented in Fig. 2. A weighted moving averaging of 5 frames was applied prior to reconstruction to reduce per-pulse signal fluctuations. For easier interpretation, the fluorescence intensity was superimposed onto the top (x-y) projection of the reconstructed OA volumes (Fig. 2(a)). OA image were normalized to the maximum value of the entire recorded image sequence. Fluorescence images were instead normalized individually to show

enhanced signal distribution within the FOV. The dashed circle indicates the effective fluorescence field of view (FOV) with a diameter of ~8 mm. Since OA is able to resolve high-resolution 3D information, different voxels along z axis can be selected for each point in the top (x-y) projection, which shows differential signal trends as a function of depth (Figs. 2(b)-(d)). Note that depth-1 is located in the most superficial area while depth-4 corresponds to the deepest location in the tumor. Due to their inherently 2D (surface-weighted) and diffuse nature, the fluorescence responses solely reveal the global signal trend across the entire tumor, i.e. sharp signal increase followed by a slow exponential decay. This is obviously associated to agent clearance from the blood circulation. Overall, the time profiles extracted from the self-normalized fluorescence images have an ascending trend, indicative of the agent accumulation in the tumor via the EPR effect. The OA signal intensity profiles at shallow regions generally correlate with the fluorescence responses, i.e. sharp decrease after Lipo-ICG bolus perfusion through the vessel followed by a slow increase (see e.g. profile p1 versus depth-1 in Fig. 2(b)). Deeper located voxels for the same x-y coordinates (depth-2 and depth-3) exhibit OA signal increase after Lipo-ICG perfusion, which appears to substantiate the observation of the EPR effect. Both fluorescence and OA signals at another superficial location (p2 in Fig. 2(c)) have a similar decreasing trend, which can be ascribed to the slow dynamics of microvascular structures. However, the OA trace at a greater depth (depth-4) remains at an elevated level after the dye perfusion, which may again correspond to Lipo-ICG leakage and accumulation via EPR. The same effect is also observed in the depth resolved OA signal traces at location p3 plotted in Fig. 2(d).

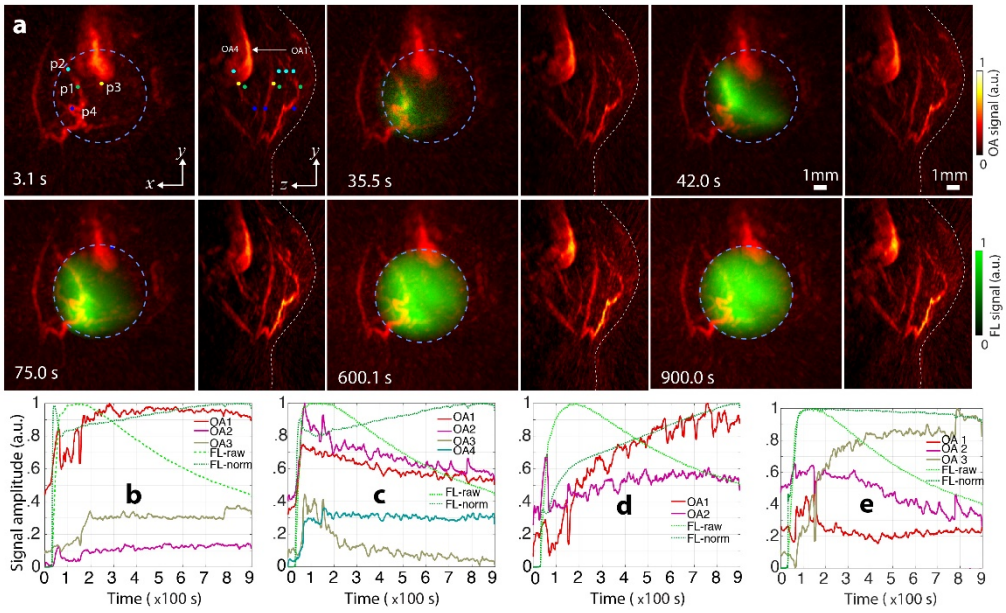

Fig. 2. Time lapse images of mouse breast tumor perfusion. (a) Maximum intensity projection of the tumor at different time points in x-y and y-z view. In the x-y view, fluorescence signal is superimposed onto the OA signal. The dotted circle indicates the effective fluorescence FOV with a diameter of ~8 mm. (b) – (d) Signal profiles from the three points p1-p3 indicated in panel (a). Note that in contrast to the surface-weighted fluorescence measurements, OA imaging can resolve 3D information, thus the OA signal traces are also plotted at different depths: depth-1 is located in the most superficial area while depth-4 corresponds to the deepest region in the tumor. Scale bar 1 mm.

Differences between perfusion profiles captured by the two modalities can be best viewed on a differential scale shown in Fig. 3. Those were calculated by subtracting the background signal taken as the average of 50 frames before injection of the agent. The light box indicates

the injection time window. Note that the images in Fig. 3 were normalized to the maximum of the corresponding sequence to better reveal the signal variations. The temporal profiles for three points of interest (p1 - p3 as indicated in Fig. 3(a)) are plotted in Figs. 3(c)-3(e). For each point, depth-1 corresponds to a superficial region while depth-2 is located at a deeper region in the tumor. A good match between the FL and OA profiles is manifested for points p1 and p2 located within main vascular structures (Figs. 3(c), (d)). However, the perfusion dynamics differs significantly in point p2 located far away from the major vasculature (Fig. 3(e)). This can be attributed to the lack of spatial and depth resolution of the FL modality, which suffers from extensive photon scattering in tissues.

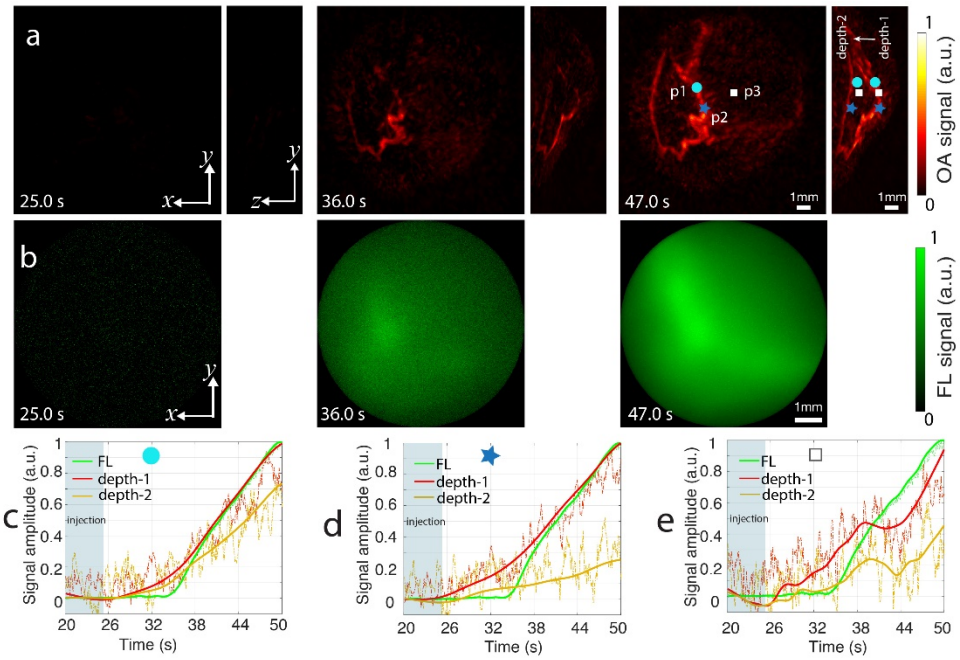

Fig. 3. Sensitivity comparison of OA and FL for Lipo-ICG detection. (a) MIPs of the OA images along the z and x directions for 3 different time points. (b) FL images for the same time points in (a). (c) – (e) Signal profiles from points p1-p3 indicated in panel (a), respectively. Scale bar 1 mm.

Figure 4 displays spectral unmixing results from the multispectral OA acquisition 30 min post Lipo-ICG injection. For the unmixing, only major endogenous chromophores were taken into consideration, namely oxy- (HbO2) and deoxy-hemoglobin (Hb), along with Lipo-ICG. As expected, the HbO2 component is predominantly concentrated in the blood vessels whereas Hb is mainly present in the tumor mass. The observed blood oxygen saturation (sO2) map is furthermore consistent with reported values, ranging from 60% to almost 100% in arteries and veins while dropping below 40% in the dermis [34]. In the unmixed Lipo-ICG image (Fig. 4(d)) the agent appears to be present both in major vessels and the tumor mass. It is important to take into account that cross-talk in the unmixing procedure may lead to erroneous interpretations, which is generally supported by the corresponding FL results shown in Fig. 4(e).

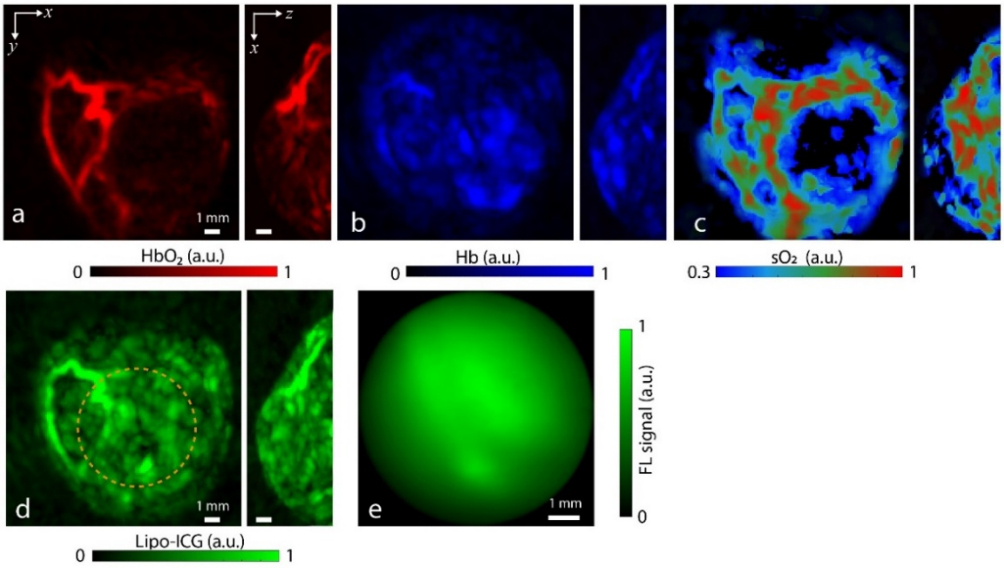

Fig. 4. Multi-spectral optoacoustic imaging of tumors 30 min post injection of the liposomal ICG agent. Maximum intensity projections (MIPs) along the depth and lateral dimensions of the unmixed distribution of oxygenated hemoglobin (a), deoxygenated hemoglobin (b), oxygen saturation (c) and liposomal ICG (d). sO2 values below 30% were set to zero. (e) Fluorescence image of the tumor with the region of interest indicated by the dotted cycle in (d).

4. Discussion and conclusions

Despite its limited penetration depth and inferior spatial resolution, planar fluorescence imaging currently remains a workhorse in cancer research e.g. through its extensive use in longitudinal molecular imaging studies looking at accumulation of drugs or targeted probes [35]. Yet, our results indicate that planar fluorescence images merely represent a surface-weighted signal integrated along different depths, which may result in misinterpretation of the underlying agent dynamics and biodistribution. The availability of InGaAs cameras has recently facilitated epi-fluorescence imaging in a new NIR window featuring less optical scattering [36] with new contrast agents having fluorescent emission in this spectral window constantly under development [37]. These developments have led to an enhancement of the resolution and contrast of epi-fluorescence images, although the inherently 2D nature of this modality still limits its quantification capabilities.

The hybrid FLOT method can facilitate more accurate interpretation of agent perfusion and biodistribution in solid tumors while also aiding the development of new nanoparticles with favorite extravasation properties and more efficient tumor targeting capacities. Since the generated ultrasound waves undergo significantly less attenuation than light for the detected frequency bandwidth, the signal decay with depth is lower for OA and hence it can potentially reach deeper regions [27]. It was further shown that tomographic imaging capacity of OA can efficiently resolve fine vascular structures in the entire tumor. The Lipo-ICG perfusion could be characterized in the sequence of OA images by analyzing the time profiles at different points of the vascular network within and around the tumor. Good correspondence to epi-fluorescence perfusion profiles was found at shallow located vessels in the tumor. However, the profiles differed significantly at deeper locations and outside major vasculature, which is attributed to the lack of depth resolution and diffuse nature of the epi-fluorescence images. Overall, the dynamic visualization of the accumulation and washout process of Lipo-ICG with the hybrid system can provide important information on the probe distribution, permeation, retention and their elimination from the body. Cross-validation between epi-

fluorescence and OAT further substantiates the observation of the EPR effect within the tumor.

Apart from monitoring of tumor perfusion and EPR effects, the FLOT system additionally allows for mapping oxygen saturation in the tumor. This may aid the characterization of tumor heterogeneity and detect low levels of oxygen partial pressure. Tumor hypoxia is one of the major causes of tumor resistance to treatments and a better characterization of its dynamic oxygenation behavior may shed light onto tumor development. The resolution of the OA system employed in this work enabled visualizing relatively large vessels in the tumor. This can be scaled by introducing a high frequency detection array [38], thus potentially enabling anatomic characterization of finer microvascular structures and neo-vascularization, an important hallmark of cancer. The hybrid system may additionally become a useful clinical tool for cancer diagnostics, intraoperative navigation or treatment monitoring [38]. While ICG is a clinically-approved small molecule dye, other agents and types of encapsulation strategies like Lipo-ICG must still overcome regulatory challenges.

In conclusion, by efficiently integrating epi-fluorescence and optoacoustic imaging, the advantages of both modalities can be synergistically exploited to provide more comprehensive and cross-validated readings of key biomarkers of tumor development. FLOT is thus expected to find broad applicability in cancer research as well as other areas involving tracking of fast biological dynamics, such as cardiac and brain imaging [41,42].

Funding

European Union's Horizon 2020 research and innovation programme under the Marie Skłodowska-Curie Grant Agreement (746430 – MSIOAM); European Research Council Consolidator Grant (ERC-2015-CoG-682379).

Acknowledgments

The authors would like to thank M. Reiss, P. Anzenhofer and U. Klemm for the assistance in animal experimentation.

Disclosures

The authors declare no competing financial interests.

References

1. S. Goel, D. G. Duda, L. Xu, L. L. Munn, Y. Boucher, D. Fukumura, and R. K. Jain, "Normalization of the vasculature for treatment of cancer and other diseases," Physiol. Rev. **91**(3), 1071–1121 (2011).
2. J. A. Nagy, L. Benjamin, H. Zeng, A. M. Dvorak, and H. F. Dvorak, "Vascular permeability, vascular hyperpermeability and angiogenesis," Angiogenesis **11**(2), 109–119 (2008).
3. R. K. Jain and T. Stylianopoulos, "Delivering nanomedicine to solid tumors," Nat. Rev. Clin. Oncol. **7**(11), 653–664 (2010).
4. D. Peer, J. M. Karp, S. Hong, O. C. Farokhzad, R. Margalit, and R. Langer, "Nanocarriers as an emerging platform for cancer therapy," Nat. Nanotechnol. **2**(12), 751–760 (2007).
5. K. Greish, "Enhanced permeability and retention (EPR) effect for anticancer nanomedicine drug targeting," Methods Mol. Biol. **624**, 25–37 (2010).
6. H. S. Choi, W. Liu, P. Misra, E. Tanaka, J. P. Zimmer, B. Itty Ipe, M. G. Bawendi, and J. V. Frangioni, "Renal clearance of quantum dots," Nat. Biotechnol. **25**(10), 1165–1170 (2007).
7. G. Song, J. S. Petschauer, A. J. Madden, and W. C. Zamboni, "Nanoparticles and the mononuclear phagocyte system: pharmacokinetics and applications for inflammatory diseases," Curr. Rheumatol. Rev. **10**(1), 22–34 (2014).
8. S. Wilhelm, A. J. Tavares, Q. Dai, S. Ohta, J. Audet, H. F. Dvorak, and W. C. W. Chan, "Analysis of nanoparticle delivery to tumours," Nat. Rev. Mater. **1**(5), 16014 (2016).
9. R. Weissleder, M. C. Schwaiger, S. S. Gambhir, and H. Hricak, "Imaging approaches to optimize molecular therapies," Sci. Transl. Med. **8**(355), 355ps16 (2016).
10. R. Weissleder and M. Nahrendorf, "Advancing biomedical imaging," Proc. Natl. Acad. Sci. U.S.A. **112**(47), 14424–14428 (2015).
11. Y. Matsumura and H. Maeda, "A new concept for macromolecular therapeutics in cancer chemotherapy: mechanism of tumoritropic accumulation of proteins and the antitumor agent smancs," Cancer Res. **46**(12 Pt 1), 6387–6392 (1986).

12. A. Karageorgis, S. Dufort, L. Sancey, M. Henry, S. Hirsjärvi, C. Passirani, J. P. Benoit, J. Gravier, I. Texier, O. Montigon, M. Benmerad, V. Siroux, E. L. Barbier, and J. L. Coll, "An MRI-based classification scheme to predict passive access of 5 to 50-nm large nanoparticles to tumors," Sci. Rep. **6**(1), 21417 (2016).
13. J. V. Frangioni, "New technologies for human cancer imaging," J. Clin. Oncol. **26**(24), 4012–4021 (2008).
14. N. Ramamonjisoa and E. Ackerstaff, "Characterization of the Tumor Microenvironment and Tumor-Stroma Interaction by Non-invasive Preclinical Imaging," Front. Oncol. **7**, 3 (2017).
15. E. Talu, K. Hettiarachchi, S. Zhao, R. L. Powell, A. P. Lee, M. L. Longo, and P. A. Dayton, "Tailoring the size distribution of ultrasound contrast agents: possible method for improving sensitivity in molecular imaging," Mol. Imaging **6**(6), 384–392 (2007).
16. G. M. van Dam, G. Themelis, L. M. Crane, N. J. Harlaar, R. G. Pleijhuis, W. Kelder, A. Sarantopoulos, J. S. de Jong, H. J. Arts, A. G. van der Zee, J. Bart, P. S. Low, and V. Ntziachristos, "Intraoperative tumor-specific fluorescence imaging in ovarian cancer by folate receptor-α targeting: first in-human results," Nat. Med. **17**(10), 1315–1319 (2011).
17. X. L. Deán-Ben, S. Gottschalk, B. Mc Larney, S. Shoham, and D. Razansky, "Advanced optoacoustic methods for multiscale imaging of in vivo dynamics," Chem. Soc. Rev. **46**(8), 2158–2198 (2017).
18. V. Ermolayev, X. L. Dean-Ben, S. Mandal, V. Ntziachristos, and D. Razansky, "Simultaneous visualization of tumour oxygenation, neovascularization and contrast agent perfusion by real-time three-dimensional optoacoustic tomography," Eur. Radiol. **26**(6), 1843–1851 (2016).
19. V. Ntziachristos and D. Razansky, "Molecular Imaging by Means of Multispectral Optoacoustic Tomography (MSOT)," Chem. Rev. **110**(5), 2783–2794 (2010).
20. P. Beard, "Biomedical photoacoustic imaging," Interface Focus **1**(4), 602–631 (2011).
21. E. Zhang, J. Laufer, and P. Beard, "Backward-mode multiwavelength photoacoustic scanner using a planar Fabry-Perot polymer film ultrasound sensor for high-resolution three-dimensional imaging of biological tissues," Appl. Opt. **47**(4), 561–577 (2008).
22. M. Xu and L. V. Wang, "Photoacoustic imaging in biomedicine," Rev. Sci. Instrum. **77**(4), 041101 (2006).
23. Y. Wang, X. Xie, X. Wang, G. Ku, K. L. Gill, D. P. O'Neal, G. Stoica, and L. V. Wang, "Photoacoustic Tomography of a Nanoshell Contrast Agent in the in Vivo Rat Brain," Nano Lett. **4**(9), 1689–1692 (2004).
24. X. Wang, Y. Pang, G. Ku, X. Xie, G. Stoica, and L. V. Wang, "Noninvasive laser-induced photoacoustic tomography for structural and functional in vivo imaging of the brain," Nat. Biotechnol. **21**(7), 803–806 (2003).
25. J. Rebling, H. Estrada, S. Gottschalk, G. Sela, M. Zwack, G. Wissmeyer, V. Ntziachristos, and D. Razansky, "Dual-wavelength hybrid optoacoustic-ultrasound biomicroscopy for functional imaging of large-scale cerebral vascular networks," J. Biophotonics **11**(9), e201800057 (2018).
26. A. Ozbek, X. L. Dean-Ben, and D. Razansky, "Optoacoustic imaging at kilohertz volumetric frame rates," Optica **5**(7), 857–863 (2018).
27. Z. Chen, X. L. Deán-Ben, S. Gottschalk, and D. Razansky, "Performance of optoacoustic and fluorescence imaging in detecting deep-seated fluorescent agents," Biomed. Opt. Express **9**(5), 2229–2239 (2018).
28. Z. Chen, X. L. Deán-Ben, S. Gottschalk, and D. Razansky, "Hybrid system for in vivo epifluorescence and 4D optoacoustic imaging," Opt. Lett. **42**(22), 4577–4580 (2017).
29. B. Mc Larney, J. Rebling, Z. Chen, X. L. Deán-Ben, S. Gottschalk, and D. Razansky, "Uniform light delivery in volumetric optoacoustic tomography," J. Biophotonics **12**(6), e201800387 (2019).
30. A. Ozbek, X. L. Dean-Ben, and D. E. N. V. Razansky, "Realtime parallel back-projection algorithm for three-dimensional optoacoustic imaging devices," in Opto-Acoustic Methods and Applications (Optical Society of America, Munich, 2013), p. 88000I.
31. S. Tzoumas, A. Nunes, I. Olefir, S. Stangl, P. Symvoulidis, S. Glasl, C. Bayer, G. Multhoff, and V. Ntziachristos, "Eigenspectra optoacoustic tomography achieves quantitative blood oxygenation imaging deep in tissues," Nat. Commun. **7**(1), 12121 (2016).
32. X. L. Deán-Ben, E. Bay, and D. Razansky, "Functional optoacoustic imaging of moving objects using microsecond-delay acquisition of multispectral three-dimensional tomographic data," Sci. Rep. **4**(1), 5878 (2015).
33. R. Cortesi, E. Esposito, S. Gambarin, P. Telloli, E. Menegatti, and C. Nastruzzi, "Preparation of liposomes by reverse-phase evaporation using alternative organic solvents," J. Microencapsul. **16**(2), 251–256 (1999).
34. S. L. Jacques, "Optical properties of biological tissues: a review," Phys. Med. Biol. **58**(11), R37–R61 (2013).
35. Y. Liu, Y. C. Tseng, and L. Huang, "Biodistribution studies of nanoparticles using fluorescence imaging: a qualitative or quantitative method?" Pharm. Res. **29**(12), 3273–3277 (2012).
36. O. T. Bruns, T. S. Bischof, D. K. Harris, D. Franke, Y. Shi, L. Riedemann, A. Bartelt, F. B. Jaworski, J. A. Carr, C. J. Rowlands, M. W. B. Wilson, O. Chen, H. Wei, G. W. Hwang, D. M. Montana, I. Coropceanu, O. B. Achorn, J. Kloepper, J. Heeren, P. T. C. So, D. Fukumura, K. F. Jensen, R. K. Jain, and M. G. Bawendi, "Next-generation in vivo optical imaging with short-wave infrared quantum dots," Nat. Biomed. Eng. **1**(4), 56 (2017).
37. E. Thimsen, B. Sadtler, and M. Berezin, "Shortwave-infrared (SWIR) emitters for biological imaging: a review of challenges and opportunities," Nanophotonics-Berlin **6**(5), 1043–1054 (2017).
38. X. L. Deán-Ben, H. López-Schier, and D. Razansky, "Optoacoustic micro-tomography at 100 volumes per second," Sci Rep-Uk **7**, 6850 (2017).
39. G. Diot, S. Metz, A. Noske, E. Liapis, B. Schroeder, S. V. Ovsepian, R. Meier, E. Rummeny, and V. Ntziachristos, "Multispectral Optoacoustic Tomography (MSOT) of Human Breast Cancer," Clin. Cancer Res. **23**(22), 6912–6922 (2017).

40. G. M. van Dam, G. Themelis, L. M. A. Crane, N. J. Harlaar, R. G. Pleijhuis, W. Kelder, A. Sarantopoulos, J. S. de Jong, H. J. G. Arts, A. G. J. van der Zee, J. Bart, P. S. Low, and V. Ntziachristos, "Intraoperative tumor-specific fluorescence imaging in ovarian cancer by folate receptor-α targeting: first in-human results," Nat. Med. **17**(10), 1315–1319 (2011).
41. H. A. Lin, X. L. Déan-Ben, M. Reiss, V. Schöttle, C. A. Wahl-Schott, I. R. Efimov, and D. Razansky, "Ultrafast Volumetric Optoacoustic Imaging of Whole Isolated Beating Mouse Heart," Sci. Rep. **8**(1), 14132 (2018).
42. S. Gottschalk, O. Degtyaruk, B. Mc Larney, J. Rebling, M. A. Hutter, X. L. Deán-Ben, S. Shoham, and D. Razansky, "Rapid volumetric optoacoustic imaging of neural dynamics across the mouse brain," Nat. Biomed. Eng. **3**(5), 392–401 (2019).